NANO LETTERS

pubs.acs.org/NanoLett Letter

Thermal Characterization of Ultrathin MgO Tunnel Barriers

Haotian Su,[§] Heungdong Kwon,[§] Fen Xue, Noriyuki Sato, Usha Bhat, Wilman Tsai, Michel Bosman, Mehdi Asheghi, Kenneth E. Goodson, Eric Pop, and Shan X. Wang*

Cite This: *Nano Lett.* 2024, 24, 14567−14573 Read Online

ACCESS | Metrics & More | Article Recommendations | Supporting Information

ABSTRACT: Magnetic tunnel junctions (MTJs) with ultrathin MgO tunnel barriers are at the heart of magnetic random-access memory (MRAM) and exhibit potential for spin caloritronics applications due to the tunnel magneto-Seebeck effect. However, the high programming current in MRAM can cause substantial heating which degrades the endurance and reliability of MTJs. Here, we report the thermal characterization of ultrathin CoFeB/MgO multilayers with total thicknesses of 4.4, 8.8, 22, and 44 nm, and with varying MgO thicknesses (1.0, 1.3, and 1.6 nm). Through time-domain thermoreflectance (TDTR) measurements and thermal modeling, we extract the intrinsic (~3.6 W m^{-1} K^{-1}) and effective (~0.85 W m^{-1} K^{-1}) thermal conductivities of annealed 1.0 nm thick MgO at room temperature. Our study reveals the thermal properties of ultrathin MgO tunnel barriers, especially the role of thermal boundary resistance, and contributes to a more precise thermal analysis of MTJs to improve the design and reliability of MRAM technologies.

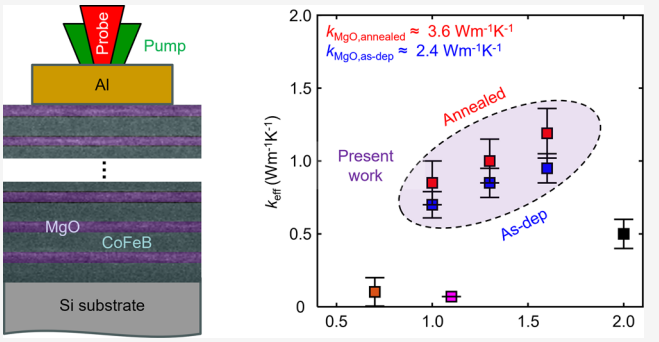

KEYWORDS: *MgO tunnel barrier, MTJ, MRAM, thermal conductivity, TDTR*

Magnetic tunnel junctions (MTJs) based on MgO are the cornerstone of spin-transfer torque magnetic random-access memory (STT-MRAM) and spin−orbit torque MRAM (SOT-MRAM).[1−5] Most commercial STT-MRAM products utilize MTJs with MgO tunnel barriers as thin as 1.0 nm and CoFeB-based free layers and reference layers.[6−9] However, it is a well-known issue that the high write current in STT-MRAM leads to significant self-heating of MgO, thereby accelerating the degradation of the MgO barrier.[10−13] Similarly, in SOT-MRAM, Joule heating in the SOT line during the write process invariably causes the temperature rise of the MTJ, contributing to the degradation of MgO as well as the diffusion of Fe and oxygen.[14−16] Although many studies have modeled the temperature rise of MgO during the writing process,[13,17−22] they often use the thermal conductivity values of bulk MgO[23] ($k_{b,MgO}$ ≈ 48 W m^{-1} K^{-1}) or those measured from relatively thick, 0.5−2 μm films[24] ($k_{f,MgO}$ ≈ 4 W m^{-1} K^{-1}) and ignore thermal boundary resistance. These deficiencies tend to result in an underestimation of the MTJ peak temperatures during MRAM operation.

Furthermore, recent years have witnessed the emergence of new spin-dependent thermal transport phenomena within magnetic nanostructures, with the tunnel magneto-Seebeck (TMS) effect in MTJs standing out as particularly interesting.[25−27] This effect could enable applications like three-dimensional thermal gradient sensing[28] or spin-polarized scanning tunneling microscopes that leverage magneto-Seebeck tunneling.[29] The TMS effect describes the dependence of the thermopower of the MTJ on its magnetic configuration under an applied thermal gradient across the MgO tunnel barrier. The thermopower is defined as $S = -U_{th}/\Delta T$, where U_{th} is the thermovoltage of the MTJ and ΔT is the temperature difference across the tunnel barrier.[25−27] Simulation of thermal transport within MTJs is a widely adopted method. Many studies have simulated the temperature difference across the ultrathin MgO barrier by using thermal conductivities of bulk or relatively thick film MgO thermal conductivity ($k_{b,MgO}$ or $k_{f,MgO}$),[26,30−35] due to the lack of experimental data on the ultrathin MgO tunnel barrier. This leads to inaccurate temperature profiles across the MgO tunnel barrier and, consequently, an overestimation of the TMS effect.

For MTJs with ultrathin MgO tunnel barriers, the effective thermal conductivity of the MgO tunnel barrier (k_{eff}) is determined by its intrinsic thermal conductivity (k_{MgO}) and the thermal boundary resistance (TBR) of the two adjoining MgO/CoFeB interfaces, R_{om}:

Received: May 31, 2024
Revised: October 17, 2024
Accepted: October 18, 2024
Published: November 6, 2024

https://doi.org/10.1021/acs.nanolett.4c02571
Nano Lett. 2024, 24, 14567−14573

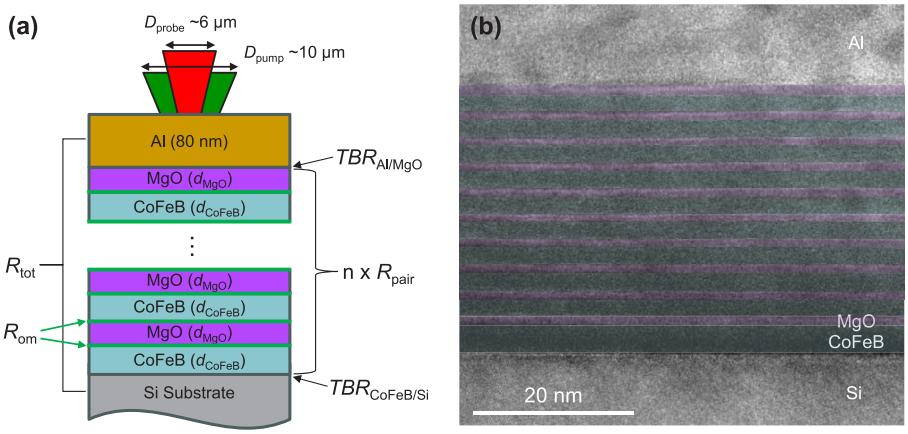

Figure 1. (a) Schematic illustrating the $[CoFeB(d_{CoFeB})/MgO(d_{MgO})]_n$ multilayers deposited for TDTR measurements, with Al transducer layer deposited on the top, where n = 2, 4, 10, 20, d_{CoFeB} = 1.2 nm, 2 nm and d_{MgO} = 1.0, 1.3, 1.6 nm in our study. (b) Colorized cross-sectional TEM image showing $[CoFeB(2.0\ nm)/MgO(1.0\ nm)]_{10}$ multilayers reveals well-defined material interfaces and the uniformity of layer thicknesses, with only minimal variations observed.

$$k_{eff} = \left(\frac{1}{k_{MgO}} + \frac{2R_{om}}{d_{MgO}}\right)^{-1}$$

We note that for ultrathin films (which may experience quasi-ballistic thermal transport), it is difficult to separate the intrinsic and interfacial contributions to the effective thermal conductivity. Thus, we generally report effective thermal conductivities (k_{eff}) for such thin layers in this work. A theoretical study with atomistic Green's functions[36] suggested that an Fe/MgO/Fe tunnel junction with a 1.0 nm MgO tunnel barrier has a $k_{eff} \approx 0.15$ W m^{-1} K^{-1} at room temperature. Experimentally, thermovoltage measurements of MTJs combined with finite-element simulations[37] have indicated that k_{eff} of a 0.7 nm thick MgO tunnel barrier is from 0.005 to 0.2 W m^{-1} K^{-1}. These indirect estimations tend to introduce considerable uncertainty.[38] In a notable advancement, Jiang et al.[39] measured the thermal properties of 2 nm thick MgO in a half-MTJ structure with a combination of time-domain thermoreflectance (TDTR) and time-resolved magneto-optic Kerr effect, estimating k_{eff} to be in the range of 0.4−0.6 W m^{-1} K^{-1}. Despite these advancements, direct thermal measurements of ultrathin MgO remain extremely challenging, primarily because such MgO tunnel barriers are just 1−2 nm thick. In addition, there are many layers of nanometer-thick films and numerous material interfaces within MTJs, which make k_{eff} extraction much more challenging.

In this study, we overcome this challenge by accurately characterizing the thermal properties of $[CoFeB/MgO]_n$ multilayers, with varying bilayer repetition n, by utilizing TDTR. We directly assess the effective thermal conductivity of MgO tunnel barriers down to 1.0 nm (k_{eff} = 0.70 ± 0.09 W m^{-1} K^{-1}), which is significantly lower than bulk or thin-film MgO thermal conductivities. We extend our analysis to explore the effects of postdeposition annealing on k_{eff}, which increases due to crystallinity induced during the annealing process. We further investigate the effect of MgO thickness on k_{eff} by varying MgO thickness from 1.0 to 1.6 nm. Our research will contribute to the ongoing efforts on the thermal optimization of STT-MRAM and SOT-MRAM[40] and the field of spin caloritronics.[27,33−35]

We deposited $[CoFeB(d_{CoFeB})/MgO(d_{MgO})]_n$ multilayers for TDTR measurements, where n = 2, 4, 10, 20; d_{CoFeB} = 1.2, 2 nm; and d_{MgO} = 1.0, 1.3, 1.6 nm, as illustrated in Figure 1a, with thermal boundary resistance (R_{om}) highlighted. A colorized cross-sectional transmission electron microscopy (TEM) image for d_{CoFeB} = 2.0 nm and d_{MgO} = 1.0 nm with n = 10 is presented in Figure 1b, providing a clear visualization of the material interfaces. The sample preparation details are given in Section S1 of the Supporting Information. We measured the total thermal resistance of the sample stack by using TDTR, which is a well-established technique[41] that has been widely adopted to measure the thermal transport properties of films. The thermophysics parameters used for fitting TDTR data are detailed in Section S2 of the Supporting Information. More details on TDTR setup and analysis can also be found in Section S2 of the Supporting Information and Kwon et al.[42]

In MTJs, CoFeB/MgO is typically deposited on metal seed layers to promote good crystallinity, with subsequent annealing commonly used to further improve the MgO texture.[43−46] In our study, we deposited CoFeB/MgO multilayers directly on a Si substrate with high and well-known thermal conductivity (Supporting Information Section S2) to avoid introducing additional materials and to enable more accurate measurements of the MgO thermal conductivity. To better emulate the real MTJ fabrication process, we also investigated the effect of postdeposition annealing on the thermal conductivity of the CoFeB/MgO films. Anneals were done at 300 °C for 30 min in a vacuum of 2.0 × 10^{-6} Torr or lower to minimize surface contamination and to improve the film crystallinity.

Figure 2a displays the representative TDTR raw data and the fitting curve for the as-deposited and annealed $[CoFeB(1.2\ nm)/MgO(1.0\ nm)]_{10}$ multilayers, offering insights into the thermal response of these multilayers under TDTR measurements. We took and analyzed such measurements from three distinct spots on all samples. TDTR time traces exhibit a clear difference between the as-deposited and annealed samples. A more rapid decay curve indicates better heat dissipation, as can be seen from the annealed samples. All fitting curves show high fitting quality, indicating the reliability of our data. Representative TDTR raw data and fitting curves for a few other measured samples are shown in Section S3 of the Supporting Information.

We conducted grazing-incident X-ray diffraction (GI-XRD) measurement of both as-deposited and annealed [CoFeB(1.2

https://doi.org/10.1021/acs.nanolett.4c02571
Nano Lett. 2024, 24, 14567−14573

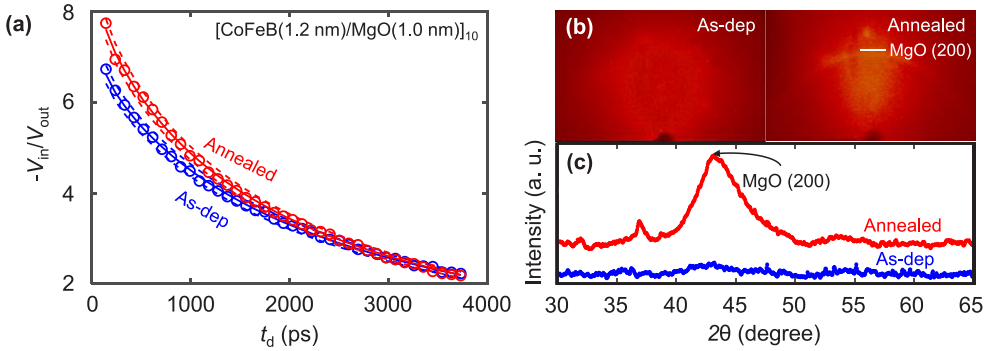

Figure 2. (a) Representative TDTR raw data (symbols) and fitted curve (lines) for the as-deposited and annealed [CoFeB(1.2 nm)/MgO(1.0 nm)]$_{10}$ multilayers; a more rapid decay curve indicates a better heat dissipation, as can be seen from the annealed sample. (b) Grazing-incident (GI)-XRD spectra and (c) corresponding GI-XRD patterns of as-deposited (amorphous) and annealed [CoFeB(1.2 nm)/MgO(1.0 nm)]$_{10}$ multilayers. The annealed sample displays the signature of the (200) textured MgO layers.

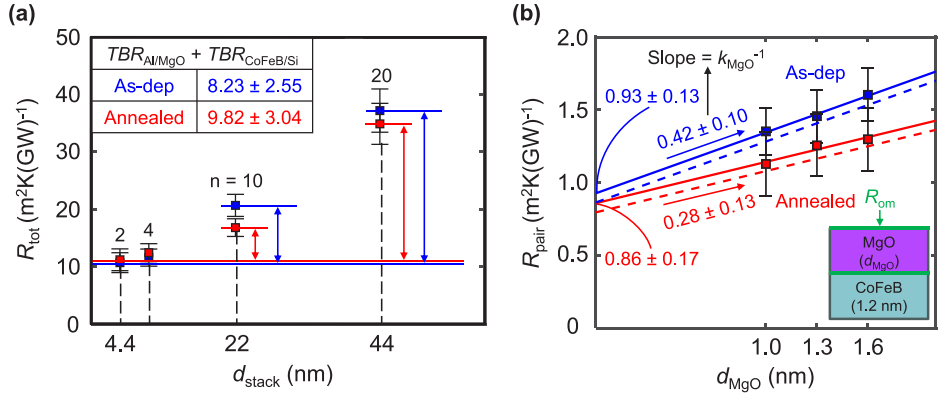

Figure 3. (a) Measured total thermal resistance (R_{tot}) of [CoFeB(1.2 nm)/MgO(1.0 nm)]$_n$ multilayers at room temperature as a function of stack total thickness (d_{stack}), where n = 2, 4, 10, 20. The TBRs at the top ($TBR_{Al/MgO}$) and bottom ($TBR_{CoFeB/Si}$) interfaces are shown in the inset table. (b) Measured R_{pair} from [CoFeB (1.2 nm)/MgO (d_{MgO})]$_{20}$ with d_{MgO} = 1.0, 1.3, and 1.6 nm, with the top and bottom interfaces TBRs substracted. The best-fit lines were plotted with gradient and vertical-intercept values indicated. The slope of each line represents $1/k_{MgO}$, while the vertical intercept shows R_{CoFeB} and $2R_{om}$. The dashed lines are plotted by removing R_{CoFeB}, showing a small contribution from the CoFeB thin film.

nm)/MgO(1.0 nm)]$_{10}$ multilayers, where the GI-XRD spectra are illustrated in Figure 2b, showing the amorphous nature of the as-deposited sample and annealed sample with (200) textured MgO. The corresponding GI-XRD patterns in Figure 2c confirm the crystallinity of the MgO layer with (200) peak at 42.9° while CoFeB remains amorphous, which agrees with the results in the literature.[43,44] All of our as-deposited films are amorphous, while MgO crystallizes after annealing, with more details in the Supporting Information. In the following sections, we will focus on the samples with d_{CoFeB} = 1.2 nm, as this thickness is closer to the thickness of the CoFeB free layer in practical applications. We find that the k_{eff} of MgO extracted from d_{CoFeB} = 2 nm falls within the k_{eff} extracted from d_{CoFeB} = 1.2 nm.

We plot the measured total thermal resistance (R_{tot}) at room temperature as a function of the [CoFeB(1.2 nm)/MgO(1.0 nm)]$_n$ multilayer total thickness in Figure 3a, with n = 2, 4, 10, and 20. A summary of measured R_{tot} can be found in Section S5 of the Supporting Information, with uncertainty analysis detailed in Section S6 of the Supporting Information. To extract the thermal resistance of one CoFeB(1.2 nm)/MgO (1.0 nm) pair (R_{pair}), we need to eliminate the effect of thermal boundary resistances (TBRs) from the top ($TBR_{Al/MgO}$) and bottom ($TBR_{CoFeB/Si}$) interfaces. The R_{tot} consists of the thermal resistance of the multilayer ($n \times R_{pair}$), as well as the TBRs at the top and bottom interfaces. We calculate R_{pair} by subtracting R_{tot} (with n = 2) from R_{tot} (n = 10 or 20), which provides the values of $8R_{pair}$ or $18R_{pair}$. Then, the TBRs from the top and bottom interfaces could be calculated by removing $2R_{pair}$ from R_{tot} (n = 2), with values shown as the inset in Figure 3a. Our results indicate that the TBRs from the top and bottom interfaces increased slightly for the annealed samples. The increased TBRs can be explained by the crystallinity of the material induced during annealing. Several studies show that thermal interfaces formed by amorphous materials have lower thermal boundary resistance than those formed by crystalline materials,[47,48] which corresponds with our as-deposited samples.

Figure 3b shows the measured R_{pair} from [CoFeB (1.2 nm)/MgO (d_{MgO})]$_{20}$ with d_{MgO} = 1.0, 1.3, and 1.6 nm for both as-deposited and annealed samples, with TBRs from top and bottom interfaces removed. R_{pair} consists of intrinsic thermal resistance from MgO ($R_{MgO} = d_{MgO}/k_{MgO}$), CoFeB ($R_{CoFeB} = d_{CoFeB}/k_{CoFeB}$), as well as two thermal boundary resistances between MgO and CoFeB interfaces (R_{om}). The thermal conductivity of one CoFeB/MgO pair (k_{pair}) is calculated from R_{pair}, $k_{pair} = (d_{CoFeB} + d_{MgO})/R_{pair}$, with the values listed in Section S5 of the Supporting Information. As we can see, k_{pair} extracted from n = 20 has a much smaller uncertainty than k_{pair} extracted from n = 10, and the former also falls within the uncertainty range of the latter. This suggests that our

https://doi.org/10.1021/acs.nanolett.4c02571
Nano Lett. 2024, 24, 14567−14573

measurement method is reliable, as we obtain consistent results with different numbers of bilayers.

As shown in Figure 3b, the best-fit lines are plotted with gradient and vertical-intercept values indicated. The uncertainties of gradient and vertical-intercept are mainly due to the systematic uncertainty in each R_{pair} at different d_{MgO}. Detailed data analyses are provided in Section S7 of the Supporting Information. The slope of each line is the inverse of the intrinsic thermal conductivity of MgO ($1/k_{MgO}$, assuming k_{MgO} does not change across this thickness range), while the vertical-intercept is the value of $R_{CoFeB} + 2R_{om}$. We find the intrinsic thermal conductivity of ultrathin as-deposited MgO film ($k_{MgO,as\text{-}dep}$) to be ~2.38 W m^{-1} K^{-1} and that of annealed MgO film ($k_{MgO,annealed}$) to be ~3.57 W m^{-1} K^{-1}.

To separate the thermal resistance of the CoFeB thin film (R_{CoFeB}) from the vertical-intercept, we measured separately the thermal conductivity of a 50 nm as-deposited CoFeB film. We found that the $k_{f,CoFeB}$ of such a film is 19.1 ± 0.6 W m^{-1} K^{-1}. We plot the dashed lines after removing R_{CoFeB}, and the resulting vertical-intercept is $2R_{om}$. This shows that the thermal boundary resistance between CoFeB and MgO (R_{om}) is significantly larger than the thermal resistance of CoFeB (R_{CoFeB}). More details of the impact of R_{CoFeB} can be found in Section S8 of the Supporting Information. It is also apparent that the vertical-intercept does not change much for the as-deposited and annealed samples, indicating a small effect of annealing on $2R_{om}$.

From the vertical-intercept of dashed lines, we find that $2R_{om}$ ≈ 0.87 m^2 K (GW)$^{-1}$ for as-deposited samples; thus, the thermal boundary conductance (TBC, i.e., $G_{om} = R_{om}^{-1}$) is ~2.3 GW m^{-2} K^{-1}. This value is higher than TBCs of typical oxide/metal interfaces, which are in the range of ~50−300 MW m^{-2} K^{-1}.[49,50] Such high TBC values found in our study could be due to the phase preserving[51−54] of phonon transmitting interfaces consisting of ultrathin films. The films are thin enough (e.g., 1.0 nm MgO represents only ~3 atomic layers) such that they are much smaller than the phonon mean free path (~6.4 nm for crystallized bulk MgO).[36] This reduces scattering events that typically disrupt phase coherence in bulk materials,[51−53] when phonons propagate through such interfaces. Phonons, as the main carriers of thermal energy in dielectric solids, can thus transmit heat more efficiently when their phase is preserved, leading to a higher TBC. Another possible reason could be due to good interfacial adhesion of sputtered films.[49,50]

To extract k_{eff} of the MgO tunnel barrier, we removed the thermal resistance of the CoFeB thin film (R_{CoFeB}) from R_{pair}. We extract and plot the k_{eff} of the MgO tunnel barrier, contributed by the intrinsic thermal conductivity of MgO (k_{MgO}) and two CoFeB/MgO thermal interfaces (R_{om}), as a function of d_{MgO}, which is shown in Figure 4. For as-deposited samples, the amorphous multilayers lack regular lattice structures, and their disordered nature leads to more phonon scattering, as well as reduced thermal conductivity compared to crystalline materials.[55−57] As a result, our as-deposited samples show lower k_{eff} values than those of annealed samples.

We also illustrate several k_{eff} values in the literature along with our data in Figure 4. The k_{eff} values in the literature are systematically lower than those from our study, which could be due to the use of bulk material thermal conductivity[37,38,58] in their calculations. However, the nanometer-thick films in the MTJ have a much lower thermal conductivity than bulk films, which leads to underestimation of k_{eff} values. For example,

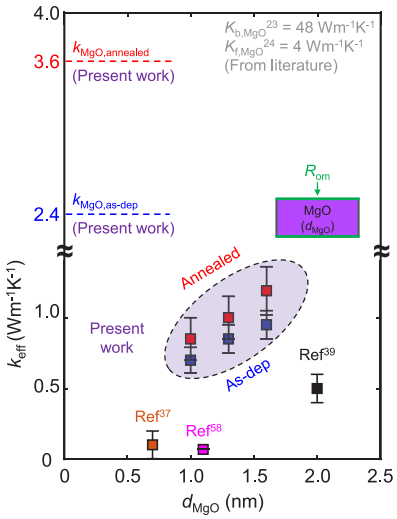

Figure 4. Extracted effective thermal conductivity of the MgO tunnel barrier (k_{eff}) at room temperature with d_{MgO} = 1.0, 1.3, and 1.6 nm, for both as-deposited and annealed samples, plotted together with several k_{eff} values from refs 37, 39, and 58. The dashed lines represent the intrinsic MgO thermal conductivity (k_{MgO}) extracted from our films. The k_{eff} value is contributed by the intrinsic thermal resistance of the MgO tunnel barrier (d_{MgO}/k_{MgO}) and two MgO/CoFeB thermal interfaces (R_{om}). The k_{eff} values for each d_{MgO} are also listed in Section S9 of the Supporting Information.

$k_{b,CoFeB}$ ≈ 87 W m^{-1} K^{-1} is widely adopted in simulations instead of the thin film value, $k_{f,CoFeB}$ ≈ 19.1 W m^{-1} K^{-1}. In contrast, our method is based on direct thermal measurement of $[CoFeB/MgO]_n$ thin films and circumvents the assumptions of *unknown* thermal properties of the various MTJ constituent thin films, which provides more accurate results. Our results show that the thermal boundary resistances between MgO and CoFeB (R_{om}) reduce the effective thermal conductivity of MgO (from k_{MgO}) but do not dominate the k_{eff}, while the k_{eff} increases slightly with MgO thickness. The k_{eff} values for each d_{MgO} are also shown in Section S9 of the Supporting Information, with uncertainty analysis details in Section S6.

In conclusion, our study provides a systematic thermal measurement and analysis of CoFeB/MgO multilayers and reports the effective thermal conductivity (k_{eff}) of as-deposited (0.70 ± 0.09 W m^{-1} K^{-1}) and annealed (0.85 ± 0.15 W m^{-1} K^{-1}) ultrathin MgO tunnel barriers down to 1.0 nm. We find surprisingly high thermal boundary conductance values between CoFeB and MgO, G_{om} ≈ 2.3 GW m^{-2} K^{-1}, much higher than those of typical oxide/metal interfaces, mainly due to phonon phase preservation across interfaces of ultrathin films. Nevertheless, non-negligible thermal interface resistances still greatly reduce k_{eff} from intrinsic MgO thermal conductivity values and should be taken into account in thermal transport analysis of such ultrathin films. Our findings suggest that self-heating in MRAM devices may be more significant than previously estimated. These results advance the understanding of thermal transport across ultrathin MgO tunnel barriers and pave the way for the thermal engineering of MRAM technologies and the development of future spin caloritronics applications.

https://doi.org/10.1021/acs.nanolett.4c02571
Nano Lett. 2024, 24, 14567−14573

■ ASSOCIATED CONTENT

Data Availability Statement

The data that support the findings of this study are available from the corresponding author upon reasonable request.

Supporting Information

The Supporting Information is available free of charge at https://pubs.acs.org/doi/10.1021/acs.nanolett.4c02571.

Sample preparation (Section S1), thermophysics parameters and TDTR setup (Section S2), representative TDTR raw data and fitting curve (Section S3), grazing-incident XRD spectra (Section S4), TDTR measurement results (Section S5), TDTR uncertainty analysis (Section S6), gradient and vertical-intercept uncertainty calculation (Section S7), impact of CoFeB thermal resistance (Section S8), effective thermal conductivity of MgO (Section S9), and discussion of experimental methods (Section S10) (PDF)

■ AUTHOR INFORMATION

Corresponding Author

Shan X. Wang − *Department of Electrical Engineering and Department of Materials Science and Engineering, Stanford University, Stanford, California 94305, United States*; Email: sxwang@stanford.edu

Authors

Haotian Su − *Department of Electrical Engineering, Stanford University, Stanford, California 94305, United States*; orcid.org/0009-0002-7113-0390

Heungdong Kwon − *Department of Mechanical Engineering, Stanford University, Stanford, California 94305, United States*; orcid.org/0000-0002-2548-3120

Fen Xue − *Department of Electrical Engineering, Stanford University, Stanford, California 94305, United States*

Noriyuki Sato − *Department of Electrical Engineering, Stanford University, Stanford, California 94305, United States*

Usha Bhat − *Department of Materials Science and Engineering, National University of Singapore, 117575, Singapore*

Wilman Tsai − *Department of Materials Science and Engineering, Stanford University, Stanford, California 94305, United States*; orcid.org/0000-0002-9259-2052

Michel Bosman − *Department of Materials Science and Engineering, National University of Singapore, 117575, Singapore*; orcid.org/0000-0002-8717-7655

Mehdi Asheghi − *Department of Mechanical Engineering, Stanford University, Stanford, California 94305, United States*

Kenneth E. Goodson − *Department of Mechanical Engineering and Department of Materials Science and Engineering, Stanford University, Stanford, California 94305, United States*

Eric Pop − *Department of Electrical Engineering, Department of Materials Science and Engineering, Department of Applied Physics, and Precourt Institute for Energy, Stanford University, Stanford, California 94305, United States*; orcid.org/0000-0003-0436-8534

Complete contact information is available at: https://pubs.acs.org/10.1021/acs.nanolett.4c02571

Author Contributions

[§]H.S. and H.K. contributed equally to this work. H.S. and S.X.W. conceived the idea. H.S. and H.K. designed the experiments. H.S. fabricated the samples and performed GI-XRD characterization with help from F.X. H.K. performed TDTR measurement. U.B. performed TEM characterization. H.S. and H.K. conducted thermal analysis with input from N.S., M.A., K.E.G., E.P., and S.X.W. H.S. and H.K. wrote the manuscript with input from F.X., W.T., M.B., M.A., K.E.G., E.P., and S.X.W. All authors discussed the results and edited the manuscript.

Notes

The authors declare no competing financial interest.

■ ACKNOWLEDGMENTS

This work was supported in part by the National Science Foundation and industry partners under grant no. 2328804 in the Future of Semiconductors (FuSe) program, grant no. 2345655 in the Partnerships for Innovation (PFI) program, and grant no. 2314591 in the Advanced Chip Engineering Design and Fabrication (ACED Fab) program. The authors also acknowledge partial support from the Stanford Non-volatile Memory Technology Research Initiative (NMTRI) Affiliates program. Part of this work was performed at the Stanford Nano Shared Facilities (SNSF), supported by the National Science Foundation under award ECCS-2026822.

■ REFERENCES

(1) Grimaldi, E.; Krizakova, V.; Sala, G.; Yasin, F.; Couet, S.; Kar, G. S.; Garello, K.; Gambardella, P. Single-shot dynamics of spin-orbit torque and spin transfer torque switching in three-terminal magnetic tunnel junctions. *Nat. Nanotechnol* **2020**, *15* (2), 111.

(2) Gupta, M.; Xiangt, Y.; García-Redondo, F.; Cai, K.; Abdi, D.; Liu, H. H.; Rao, S.; Hiblot, G.; Couet, S.; García-Bardon, M.; Hellings, G. Ultimate MRAM Scaling: Design Exploration of High-Density, High-Performance and Energy-Efficient VGSOT for Last Level Cache. In *2023 IEEE International Electron Devices Meeting (IEDM)*, 2023, DOI: 10.1109/IEDM45741.2023.10413886.

(3) Li, K.-S.; Shieh, J.-M.; Chen, Y.-J.; Hsu, C.-L.; Shen, C.-H.; Hou, T.-H.; Lin, C.-P.; Lai, C.-H.; Tang, D. D.; Yuan-Chen Sun, J. First BEOL-compatible, 10 ns-fast, and Durable 55 nm Top-pSOT-MRAM with High TMR (>130%). In *2023 IEEEInternational Electron Devices Meeting (IEDM)*, 2023, DOI: 10.1109/IEDM45741.2023.10413685.

(4) Garello, K.; Yasin, F.; Couet, S.; Souriau, L.; Swerts, J.; Rao, S.; Van Beek, S.; Kim, W.; Liu, E.; Kundu, S.; et al.. SOT-MRAM 300MM Integration for Low Power and Ultrafast Embedded Memories. In *2018 IEEE Symposium on VLSI Circuits*, 2018, DOI: 10.1109/VLSIC.2018.8502269.

(5) Van Beek, S.; Cai, K.; Yasin, F.; Hody, H.; Talmelli, G.; Nguyen, V. D.; Vergel, N. F.; Palomino, A.; Trovato, A.; Wostyn, K.; et al.. Scaling the SOT track−A path towards maximizing efficiency in SOT-MRAM. In *2023 International Electron Devices Meeting (IEDM)*, 2023, DOI: 10.1109/IEDM45741.2023.10413749.

(6) Sato, H.; Honjo, H.; Watanabe, T.; Niwa, M.; Koike, H.; Miura, S.; Saito, T.; Inoue, H.; Nasuno, T.; Tanigawa, T.; et al.. 14ns write speed 128Mb density Embedded STT-MRAM with endurance > 10^{10} and 10yrs retention@85°C using novel low damage MTJ integration process. In *2018 IEEE International Electron Devices Meeting (IEDM)*, 2018, DOI: 10.1109/IEDM.2018.8614606.

(7) Worledge, D. C. Spin-Transfer-Torque MRAM: the Next Revolution in Memory. In *2022 IEEE International Memory Workshop (IMW)EEE*, 2022 DOI: 10.1109/Imw52921.2022.9779288.

(8) Golonzka, O.; Alzate, J. G.; Arslan, U.; Bohr, M.; Bai, P.; Brockman, J.; Buford, B.; Connor, C.; Das, N.; Doyle, B.; et al.. MRAM as Embedded Non-Volatile Memory Solution for 22FFL

FinFET Technology. In *2018 IEEE International Electron Devices Meeting (IEDM)*, 2018, DOI: 10.1109/IEDM.2018.8614620.
(9) Song, M. Y.; Chen, K. L.; Chen, K. M.; Chang, K. T.; Wang, I. J.; Hsin, Y. C.; Lin, C. Y.; Ambrosi, E.; Khwa, W.-S.; Lu, Y. L.; et al.. High RA Dual-MTJ SOT-MRAM devices for High Speed (10ns) Compute-in-Memory Applications. In *2023 International Electron Devices Meeting (IEDM)*, 2023, DOI: 10.1109/IEDM45741.2023.10413832.
(10) Hosotani, K.; Nagamine, M.; Ueda, T.; Aikawa, H.; Ikegawa, S.; Asao, Y.; Yoda, H.; Nitayama, A. Effect of Self-Heating on Time-Dependent Dielectric Breakdown in Ultrathin MgO Magnetic Tunnel Junctions for Spin Torque Transfer Switching Magnetic Random Access Memory. *Jpn. J. Appl. Phys.* **2010**, *49* (4S), 04DD15.
(11) Van Beek, S.; O'Sullivan, B. J.; Roussel, P. J.; Degraeve, R.; Bury, E.; Swerts, J.; Couet, S.; Souriau, L.; Kundu, S.; Rao, S.; et al.. Impact of self-heating on reliability predictions in STT-MRAM. In *2018 IEEE International Electron Devices Meeting (IEDM)*, 2018, DOI: 10.1109/IEDM.2018.8614617.
(12) Wang, Y.; Cai, H.; Naviner, L. A. D.; Zhang, Y.; Zhao, X. X.; Deng, E.; Klein, J. O.; Zhao, W. S. Compact Model of Dielectric Breakdown in Spin-Transfer Torque Magnetic Tunnel Junction. *IEEE Trans. Electron Devices* **2016**, *63* (4), 1762−1767.
(13) Zhang, X.; Zhang, G.; Shen, L.; Yu, P.; Jiang, Y. Life-time degradation of STT-MRAM by self-heating effect with TDDB model. *Solid-State Electron.* **2020**, *173*, 107878.
(14) Van Beek, S.; Cai, K.; Rao, S.; Jayakumar, G.; Couet, S.; Jossart, N.; Chasin, A.; Kar, G. S. MTJ degradation in SOT-MRAM by self-heating-induced diffusion. *2022 IEEE International Reliability Physics Symposium (IRPS)* **2022**.
(15) Van Beek, S.; Cai, K. M.; Fan, K. Q.; Talmelli, G.; Trovato, A.; Jossart, N.; Rao, S.; Chasin, A.; Couet, S. MTJ degradation in multi-pillar SOT-MRAM with selective writing. *2023 IEEE International Reliability Physics Symposium (IRPS)* **2023**.
(16) Van Beek, S.; Kateel, V.; Cai, K.; Jossart, N.; Rao, S.; Couet, S. Impact of SOT & STT stress on MTJ degradation in SOT-MRAM. In *2023 IEEE International Magnetic Conference - Short Papers (INTERMAG Short Papers)*, 2023, DOI: 10.1109/INTERMAG-ShortPapers58606.2023.10228201.
(17) Teso, B.; Siritaratiwat, A.; Kaewrawang, A.; Kruesubthaworn, A.; Namvong, A.; Sainon, S.; Surawanitkun, C. Switching Performance Comparison With Low Switching Energy Due to Initial Temperature Increment in CoFeB/MgO-Based Single and Double Barriers. *IEEE Trans. Electron Devices* **2019**, *66* (9), 4062−4067.
(18) NamKoong, J. H.; Lim, S. H. Temperature increase in nanostructured cells of a magnetic tunnel junction during current-induced magnetization switching. *J. Phys. D: Appl. Phys.* **2009**, *42* (22), 225003.
(19) Lim, J. H.; Raghavan, N.; Mei, S.; Naik, V. B.; Kwon, J. H.; Noh, S. M.; Liu, B.; Toh, E. H.; Chung, N. L.; Chao, R.; et al.. Area and pulsewidth dependence of bipolar TDDB in MgO magnetic tunnel junction. In *2018 IEEE International Reliability Physics Symposium (IRPS)*, 2018, DOI: 10.1109/IRPS.2018.8353637.
(20) Rehm, L.; Wolf, G.; Kardasz, B.; Cogulu, E.; Chen, Y.; Pinarbasi, M.; Kent, A. D. Thermal Effects in Spin-Torque Switching of Perpendicular Magnetic Tunnel Junctions at Cryogenic Temperatures. *Phys. Rev. Appl.* **2021**, *15* (3), 034088.
(21) Choi, C.-M.; Oh, Y.-T.; Kim, K.-J.; Park, J.-S.; Sukegawa, H.; Mitani, S.; Kim, S.-K.; Lee, J.-Y.; Song, Y.-H. Temperature dependence of reliability characteristics for magnetic tunnel junctions with a thin MgO dielectric film. *Semicond. Sci. Technol.* **2016**, *31* (7), 075004.
(22) Choi, C.-M.; Sukegawa, H.; Mitani, S.; Song, Y.-H. TDDB modeling depending on interfacial conditions in magnetic tunnel junctions. *Semicond. Sci. Technol.* **2017**, *32* (10), 105007.
(23) Slack, G. A. Thermal Conductivity of MgO,Al2O3, MgAl2O4, andFe3O4Crystals from 3° to 300 K. *Phys. Rev.* **1962**, *126* (2), 427−441.
(24) Lee, S. M.; Cahill, D. G.; Allen, T. H. Thermal-Conductivity of Sputtered Oxide-Films. *Phys. Rev. B* **1995**, *52* (1), 253−257.
(25) Walter, M.; Walowski, J.; Zbarsky, V.; Münzenberg, M.; Schäfers, M.; Ebke, D.; Reiss, G.; Thomas, A.; Peretzki, P.; Seibt, M.; et al. Seebeck effect in magnetic tunnel junctions. *Nat. Mater.* **2011**, *10* (10), 742−746.
(26) Lv, H.; Fidalgo, J.; Kampfe, T.; Langer, J.; Wrona, J.; Ocker, B.; Freitas, P. P.; Cardoso, S. Seebeck effect and Joule heating in CoFeB/MgO/CoFeB-based perpendicular magnetic tunnel junctions with low resistance area product. *J. Phys. D: Appl. Phys.* **2022**, *55* (26), 265302.
(27) Kuschel, T.; Czerner, M.; Walowski, J.; Thomas, A.; Schumacher, H. W.; Reiss, G.; Heiliger, C.; Münzenberg, M. Tunnel magneto-Seebeck effect. *J. Phys. D: Appl. Phys.* **2019**, *52* (13), 133001.
(28) Martens, U.; Huebner, T.; Ulrichs, H.; Reimer, O.; Kuschel, T.; Tamming, R. R.; Chang, C.-L.; Tobey, R. I.; Thomas, A.; Münzenberg, M.; Walowski, J. Anomalous Nernst effect and three-dimensional temperature gradients in magnetic tunnel junctions. *Communications Physics* **2018**, *1* (1), 65.
(29) Friesen, C.; Osterhage, H.; Friedlein, J.; Schlenhoff, A.; Wiesendanger, R.; Krause, S. Magneto-Seebeck tunneling on the atomic scale. *Science* **2019**, *363* (6431), 1065−1067.
(30) Bohnert, T.; Serrano-Guisan, S.; Paz, E.; Lacoste, B.; Ferreira, R.; Freitas, P. P. Magnetic tunnel junctions with integrated thermometers for magnetothermopower measurements. *J. Phys.: Condens. Matter* **2017**, *29* (18), 185303.
(31) Liebing, N.; Serrano-Guisan, S.; Rott, K.; Reiss, G.; Langer, J.; Ocker, B.; Schumacher, H. W. Determination of spin-dependent Seebeck coefficients of CoFeB/MgO/CoFeB magnetic tunnel junction nanopillars. *J. Appl. Phys.* **2012**, *111* (7), 07C520.
(32) Cansever, H.; Lindner, J.; Huebner, T.; Niesen, A.; Reiss, G.; Fassbender, J.; Deac, A. M. Characterization of Continuous Wave Laser-Induced Thermal Gradients in Magnetic Tunnel Junctions Integrated Into Microresonators via COMSOL Simulations. *IEEE Transactions on Magnetics* **2019**, *55* (7), 1−5.
(33) Liebing, N.; Serrano-Guisan, S.; Rott, K.; Reiss, G.; Langer, J.; Ocker, B.; Schumacher, H. W. Tunneling magnetothermopower in magnetic tunnel junction nanopillars. *Phys. Rev. Lett.* **2011**, *107* (17), No. 177201.
(34) Huebner, T.; Martens, U.; Walowski, J.; Boehnke, A.; Krieft, J.; Heiliger, C.; Thomas, A.; Reiss, G.; Kuschel, T.; Münzenberg, M. Enhancement of thermovoltage and tunnel magneto-Seebeck effect in CoFeB-based magnetic tunnel junctions by variation of the MgAl2O4 and MgO barrier thickness. *Phys. Rev. B* **2017**, *96* (21), 214435.
(35) Liand, S.; Jiang, Y. Nanoscale Thermal Transport Model of Magnetic Tunnel Junction (MTJ) Device for STT-MRAM. *IEEE Transactions on Magnetics* **2022**, *58* (8), 1−6.
(36) Zhang, J.; Bachman, M.; Czerner, M.; Heiliger, C. Thermal Transport and Nonequilibrium Temperature Drop Across a Magnetic Tunnel Junction. *Phys. Rev. Lett.* **2015**, *115* (3), No. 037203.
(37) Böhnert, T.; Dutra, R.; Sommer, R. L.; Paz, E.; Serrano-Guisan, S.; Ferreira, R.; Freitas, P. P. Influence of the thermal interface resistance on the thermovoltage of a magnetic tunnel junction. *Phys. Rev. B* **2017**, *95* (10), 104441.
(38) Huebner, T.; Martens, U.; Walowski, J.; Münzenberg, M.; Thomas, A.; Reiss, G.; Kuschel, T. Thermal conductivity of thin insulating films determined by tunnel magneto-Seebeck effect measurements and finite-element modeling. *J. Phys. D: Appl. Phys.* **2018**, *51* (22), 224006.
(39) Jang, H.; Marnitz, L.; Huebner, T.; Kimling, J.; Kuschel, T.; Cahill, D. G. Thermal Conductivity of Oxide Tunnel Barriers in Magnetic Tunnel Junctions Measured by Ultrafast Thermoreflectance and Magneto-Optic Kerr Effect Thermometry. *Phys. Rev. Appl.* **2020**, *13* (2), 024007.
(40) Su, H.; Kwon, H.; Hwang, W.; Xue, F.; Köroğlu, Ç.; Tsai, W.; Asheghi, M.; Goodson, K. E.; Wang, S. X.; Pop, E. Thermal Optimization of Two-Terminal SOT-MRAM. *J. Appl. Phys.* **2024**, *136* (1), 0211620.
(41) Jiang, P.; Qian, X.; Yang, R. Tutorial: Time-domain thermoreflectance (TDTR) for thermal property characterization of bulk and thin film materials. *J. Appl. Phys.* **2018**, *124* (16), 161103.

(42) Kwon, H.; Khan, A. I.; Perez, C.; Asheghi, M.; Pop, E.; Goodson, K. E. Uncovering Thermal and Electrical Properties of Sb(2)Te(3)/GeTe Superlattice Films. *Nano Lett.* **2021**, *21* (14), 5984−5990.
(43) Park, C.; Wang, Y. H.; Laughlin, D. E.; Zhu, J. G. Effect of Adjacent Layers on Crystallization and Magnetoresistance in CoFeB/MgO/CoFeB Magnetic Tunnel Junction. *IEEE Transactions on Magnetics* **2006**, *42* (10), 2639−2641.
(44) Bhusan Singh, B.; Chaudhary, S. Effect of MgO spacer and annealing on interface and magnetic properties of ion beam sputtered NiFe/Mg/MgO/CoFe layer structures. *J. Appl. Phys.* **2012**, *112* (6), 063906.
(45) Souza, M. M. C.; Sousa, R. C.; Ducruet, C.; Auffret, S.; Dieny, B. Metallic Mg insertion in rf deposited MgO barrier. *J. Appl. Phys.* **2010**, *107* (9), 09C702.
(46) Tsunekawa, K.; Djayaprawira, D. D.; Nagai, M.; Maehara, H.; Yamagata, S.; Watanabe, N.; Yuasa, S.; Suzuki, Y.; Ando, K. Giant tunneling magnetoresistance effect in low-resistance CoFeB/MgO(001)/CoFeB magnetic tunnel junctions for read-head applications. *Appl. Phys. Lett.* **2005**, *87* (7), 072503.
(47) Giri, A.; King, S. W.; Lanford, W. A.; Mei, A. B.; Merrill, D.; Li, L.; Oviedo, R.; Richards, J.; Olson, D. H.; Braun, J. L.; et al. Interfacial Defect Vibrations Enhance Thermal Transport in Amorphous Multilayers with Ultrahigh Thermal Boundary Conductance. *Adv. Mater.* **2018**, *30* (44), No. e1804097.
(48) Kimling, J.; Philippi-Kobs, A.; Jacobsohn, J.; Oepen, H. P.; Cahill, D. G. Thermal conductance of interfaces with amorphous SiO2 measured by time-resolved magneto-optic Kerr-effect thermometry. *Phys. Rev. B* **2017**, *95* (18), 184305.
(49) Monachon, C.; Weber, L.; Dames, C. Thermal Boundary Conductance: A Materials Science Perspective. *Annu. Rev. Mater. Res.* **2016**, *46*, 433.
(50) Cahill, D. G.; Braun, P. V.; Chen, G.; Clarke, D. R.; Fan, S.; Goodson, K. E.; Keblinski, P.; King, W. P.; Mahan, G. D.; Majumdar, A. Nanoscale thermal transport. II. 2003−2012. *Appl. Phys. Rev.* **2014**, *1* (1), 011305.
(51) Chen, G. Thermal conductivity and ballistic-phonon transport in the cross-plane direction of superlattices. *Phys. Rev. B* **1998**, *57* (23), 14958−14973.
(52) Ravichandran, J.; Yadav, A. K.; Cheaito, R.; Rossen, P. B.; Soukiassian, A.; Suresha, S. J.; Duda, J. C.; Foley, B. M.; Lee, C. H.; Zhu, Y.; et al. Crossover from incoherent to coherent phonon scattering in epitaxial oxide superlattices. *Nat. Mater.* **2014**, *13* (2), 168−172.
(53) Chen, G. Non-Fourier phonon heat conduction at the microscale and nanoscale. *Nature Reviews Physics* **2021**, *3* (8), 555−569.
(54) Wang, Y.; Huang, H.; Ruan, X. Decomposition of coherent and incoherent phonon conduction in superlattices and random multilayers. *Phys. Rev. B* **2014**, *90* (16), 165406.
(55) Einstein, A. Elementare Betrachtungen über die thermische Molekularbewegung in festen Körpern. *Annalen der Physik* **1911**, *340* (9), 679−694.
(56) Slack, G. A. The Thermal Conductivity of Nonmetallic Crystals. *Solid State Physics* **1979**, *34*, 1−71.
(57) Wingert, M. C.; Zheng, J.; Kwon, S.; Chen, R. Thermal transport in amorphous materials: a review. *Semicond. Sci. Technol.* **2016**, *31* (11), 113003.
(58) Goto, M.; Wakatake, Y.; Oji, U. K.; Miwa, S.; Strelkov, N.; Dieny, B.; Kubota, H.; Yakushiji, K.; Fukushima, A.; Yuasa, S.; Suzuki, Y. Microwave amplification in a magnetic tunnel junction induced by heat-to-spin conversion at the nanoscale. *Nat. Nanotechnol* **2019**, *14* (1), 40−43.

https://doi.org/10.1021/acs.nanolett.4c02571
Nano Lett. 2024, 24, 14567−14573

SUPPORTING INFORMATION

Thermal Characterization of Ultrathin MgO Tunnel Barriers

Haotian Su[1], Heungdong Kwon[2], Fen Xue[1], Noriyuki Sato[1], Usha Bhat[3], Wilman Tsai[4], Michel Bosman[3], Mehdi Asheghi[2], Kenneth E. Goodson[2,4], Eric Pop[1,4,5,6], and Shan X. Wang[1,4,a)]

[1]Department of Electrical Engineering, Stanford University, Stanford, CA 94305, USA

[2]Department of Mechanical Engineering, Stanford University, Stanford, CA 94305, USA

[3]Department of Materials Science and Engineering, National University of Singapore, 117575, Singapore

[4]Department of Materials Science and Engineering, Stanford University, Stanford, CA 94305, USA

[5]Department of Applied Physics, Stanford University, Stanford, CA 94305, USA

[6]Precourt Institute for Energy, Stanford University, CA 94305, USA

[a)]Author to whom correspondence should be addressed: sxwang@stanford.edu

S1. Sample Preparation

We deposited $[Co_{20}Fe_{60}B_{20}(d_{CoFeB})/MgO(d_{MgO})]_n$ multilayers on highly resistive Si substrate at room temperature in an AJA magnetron sputtering system with a base pressure of 2.0×10^{-8} Torr or lower, where n = 2, 4, 10, 20, d_{CoFeB} = 1.2, 2 nm and d_{MgO} = 1.0, 1.3, 1.6 nm. A 200 Oersted magnetic field generated by the N-S magnets attached to the wafer holder was applied during the deposition of all films. CoFeB was DC sputtered at 25 W at 2 mTorr Argon atmosphere, with deposition rate at 4.8 Å/min. The MgO layer was RF sputtered at 100 W and 0.6 mTorr Argon atmosphere, with a deposition rate of 1.25 Å/min. Aluminum (Al) transducer layer for thermal measurements was evaporated using Kurt J. Lesker E-beam Evaporator at Stanford Nano Shared Facilities (SNSF), with base pressure at 5.0×10^{-8} Torr and rate at 1 Å/s. We calibrated the deposition rate for all the above depositions using X-ray reflectivity. To ensure consistency in our experiments, an 80 nm-thick Al transducer layer was deposited simultaneously on all as-deposited and annealed samples.

S2. Thermophysics Parameters and TDTR Setup

The thermophysics parameters used for fitting time-domain thermoreflectance (TDTR) data are listed in the **Table S1** below. In our experiment, a mode-locked Nd:YVO_4 laser produces ~ 10 ps pulses at the wavelength of 1064 nm with 82.3 MHz repetition rate. The beam splits into a frequency-doubled pump beam modulated at 9 MHz, which heats the surface of the Al transducer and thus establishes a transient temperature field within the sample. The surface temperature of the Al transducer layer is subsequently assessed using an optically delayed probe beam. The reflected probe beam from the sample is monitored by a fast photodiode detector. The TDTR measurement relies on the principle that the reflectivity of the metallic surface is proportional to its temperature. The co-aligned pump and probe beams are focused on the sample surface with Gaussian waist diameters of ~ 10 μm and ~ 6 μm, respectively, as illustrated in **Figure 1a** in the manuscript.

Table S1. Thermophysics parameters utilized in TDTR analysis in our study. These parameters include the pump beam modulation frequency (f_m), and the thermal conductivities of Al (k_{Al}) and Si (k_{Si}). Additionally, the volumetric heat capacities of Al ($C_{v,Al}$),[1] MgO ($C_{v,MgO}$),[2] CoFeB ($C_{v,CoFeB}$),[2] and Si ($C_{v,Si}$)[3] are taken from the literature. All thermal conductivities and heat capacities are listed at room temperature.

TDTR parameters	Values
f_m	9 MHz
k_{Al}	160 $Wm^{-1}K^{-1}$
k_{Si}	134 $Wm^{-1}K^{-1}$
$C_{v,Al}$[1]	2.43 $MJ{\cdot}m^{-3}K^{-1}$
$C_{v,MgO}$[2]	3.36 $MJ{\cdot}m^{-3}K^{-1}$
$C_{v,CoFeB}$[2]	3.30 $MJ{\cdot}m^{-3}K^{-1}$
$C_{v,Si}$[3]	1.65 $MJ{\cdot}m^{-3}K^{-1}$

S3. Representative TDTR Data and Fitting Curve

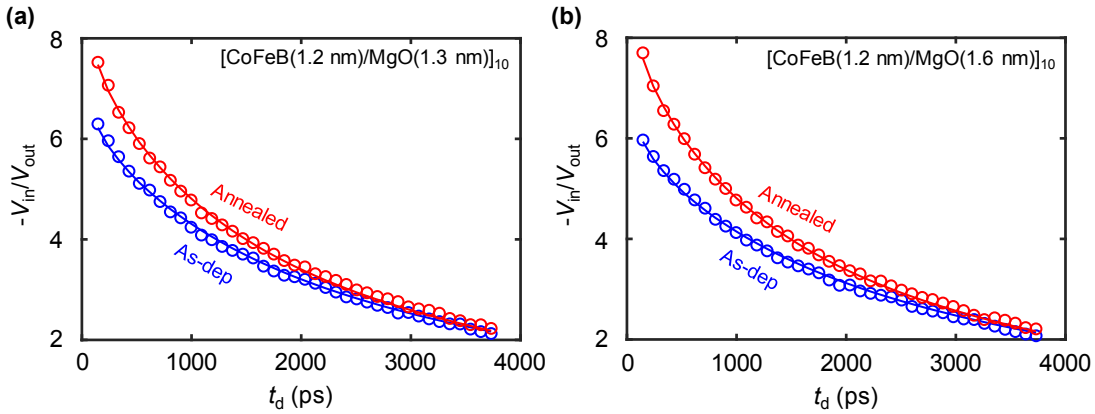

Figure S1. Representative TDTR data (symbols) and the fitting curve (lines) for the as-deposited and annealed [CoFeB(1.2 nm)/MgO(d_{MgO})]$_{10}$ multilayers, with **(a)** d_{MgO} = 1.3 nm and **(b)** 1.6 nm.

S4. Grazing-Incident XRD Spectra

We conducted X-ray diffraction (XRD) measurements on the samples, by using a Bruker D8 Venture single crystal diffractometer with Cu Ka (8.04 keV) radiation in grazing incidence geometry, following the same method in Xue *et al*.[4] **Figure S2** shows the grazing-incident (GI)-XRD spectra of as-deposited and annealed [CoFeB(1.2 nm)/MgO(d_{MgO})]$_{10}$ multilayers with MgO thickness of (a) 1.3 nm and (b) 1.6 nm, showing as-deposited sample with amorphous nature and annealed sample with (200) textured MgO.

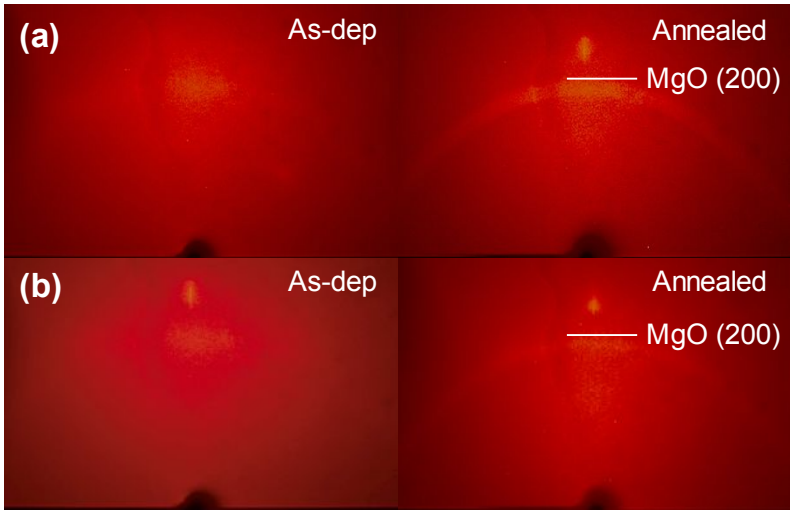

Figure S2. GI-XRD spectra of as-deposited and annealed [CoFeB(1.2 nm)/MgO(d_{MgO})]$_{10}$ multilayers with d_{MgO} of **(a)** 1.3 nm and **(b)** 1.6 nm.

S5. TDTR Measurement Results

Table S2. A summary of measured total thermal resistance (R_{tot}), as well as the intrinsic thermal conductivity of CoFeB(1.2 nm)/MgO(d_{MgO}) pair. k_{pair} equals to (d_{CoFeB} + d_{MgO})/R_{pair}, has much smaller uncertainty when derived from n = 20 than from n = 10, with error analysis details in **Section S6**.

Sample	R_{tot} (m^{2}K(GW)$^{-1}$)	k_{pair} (Wm^{-1}K^{-1})
[CoFeB(1.2 nm)/MgO(1.0 nm)]$_2$ As-dep	10.72 ± 1.66	-
[CoFeB(1.2 nm)/MgO(1.0 nm)]$_2$ Annealed	11.23 ± 1.82	-
[CoFeB(1.2 nm)/MgO(1.0 nm)]$_4$ As-dep	11.60 ± 1.40	-
[CoFeB(1.2 nm)/MgO(1.0 nm)]$_4$ As-dep	12.47 ± 1.45	-
[CoFeB(1.2 nm)/MgO(1.0 nm)]$_{10}$ As-dep	20.70 ± 1.88	1.76 ± 0.45
[CoFeB(1.2 nm)/MgO(1.0 nm)]$_{10}$ Annealed	16.83 ± 2.19	3.14 ± 1.60
[CoFeB(1.2 nm)/MgO(1.0 nm)]$_{20}$ As-dep	37.21 ± 2.65	1.48 ± 0.18
[CoFeB(1.2 nm)/MgO(1.0 nm)]$_{20}$ Annealed	34.91 ± 2.63	1.77 ± 0.29
[CoFeB(1.2 nm)/MgO(1.3 nm)]$_{10}$ As-dep	22.73 ± 1.79	1.72 ± 0.44
[CoFeB(1.2 nm)/MgO(1.3 nm)]$_{10}$ Annealed	16.52 ± 1.60	3.74 ± 1.85
[CoFeB(1.2 nm)/MgO(1.3 nm)]$_{20}$ As-dep	39.32 ± 2.57	1.58 ± 0.20
[CoFeB(1.2 nm)/MgO(1.3 nm)]$_{20}$ Annealed	37.48 ± 2.65	1.83 ± 0.27
[CoFeB(1.2 nm)/MgO(1.6 nm)]$_{10}$ As-dep	24.39 ± 1.89	1.73 ± 0.36
[CoFeB(1.2 nm)/MgO(1.6 nm)]$_{10}$ Annealed	16.19 ± 1.65	4.40 ± 2.29
[CoFeB(1.2 nm)/MgO(1.6 nm)]$_{20}$ As-dep	42.26 ± 2.59	1.62 ± 0.18
[CoFeB(1.2 nm)/MgO(1.6 nm)]$_{20}$ Annealed	38.34 ± 2.46	2.00 ± 0.27

S6. TDTR Uncertainty Analysis

Table S3. Sources of uncertainty and corresponding values assumed in TDTR error propagation analysis.

Source of uncertainty	Value
Laser spot size	5%
k_{Al}	15%
k_{Si}	6 $Wm^{-1}K^{-1}$
d_{Al}	2 nm
d_{stack}	2%
$C_{v,Al}$	2%
$C_{v,ML}$	2%
$C_{v,Si}$	2%

To quantify the error (δ) in the measured total thermal resistance (R_{tot}) obtained from the data fitting of TDTR response, we conducted an error propagation analysis.[5,6] The δ of the measured R_{tot} propagates from the uncertainties of the parameters used in the TDTR fitting procedure. The uncertainty of each parameter is tabulated in **Table S3**. All the individual errors are summed in the quadrature. As R_{tot} (n = 2) is subtracted from R_{tot} (n = 10 or 20), which provides the $8R_{pair}$ or $18R_{pair}$, the error of R_{pair} is calculated as:

$$\delta_{R_{\mathrm{pair}(n=8 \text{ or } 18)}} = \sqrt{\delta^2_{R_{\mathrm{tot}(n=2)}} + \delta^2_{R_{\mathrm{tot}(n=10 \text{ or } 20)}}}$$

The thermal conductivity of one CoFeB/MgO pair (k_{pair}), can be calculated by $k_{pair} = d_{pair(n=8 \text{ or } 18)} / R_{pair(n = 8 \text{ or } 18)}$, where $d_{pair} = d_{CoFeB} + d_{MgO}$. Thus, the error of k_{pair} is calculated as follows:

$$\delta_{k_{\mathrm{pair}}} = k_{\mathrm{pair}} \sqrt{\left(\frac{\delta_{d_{\mathrm{pair}(n=8 \text{ or } 18)}}}{d_{\mathrm{pair}(n=8 \text{ or } 18)}}\right)^2 + \left(\frac{\delta_{R_{\mathrm{pair}(n=8 \text{ or } 18)}}}{R_{\mathrm{pair}(n=8 \text{ or } 18)}}\right)^2}$$

The corresponding thermal resistance of one CoFeB/MgO pair can be calculated by d_{pair}/k_{pair} and its error can be calculated similarly:

$$\delta_{R_{\mathrm{pair}}} = R_{\mathrm{pair}} \sqrt{\left(\frac{\delta_{d_{\mathrm{pair}(n=8 \text{ or } 18)}}}{d_{\mathrm{pair}(n=8 \text{ or } 18)}}\right)^2 + \left(\frac{\delta_{k_{\mathrm{pair}}}}{k_{\mathrm{pair}}}\right)^2}$$

The thermal boundary resistances at the top ($TBR_{CoFeB/Si}$) and bottom ($TBR_{MgO/Al}$) interfaces are extracted by subtracting $2R_{pair}$ from R_{tot} (n = 2). The error is calculated as:

$$\delta_{TBR_{\mathrm{Al/MgO}}+TBR_{\mathrm{CoFeB/Si}}} = (TBR_{\mathrm{Al/MgO}} + TBR_{\mathrm{CoFeB/Si}}) \sqrt{\left(\frac{\delta_{2 \times R_{\mathrm{pair}}}}{2 \times R_{\mathrm{pair}}}\right)^2 + \left(\frac{\delta_{R_{\mathrm{tot}(n=2)}}}{R_{\mathrm{tot}(n=2)}}\right)^2}$$

The calculated error of the TBRs at the top and bottom interfaces is added to the error of k_{eff}, as the TBR is subtracted from the R_{tot} of the multilayer. The error of k_{eff} can be calculated below:

$$\delta_{k_{\text{eff}}} = k_{\text{eff}} \sqrt{\left(\frac{\delta_{d_{\text{MgO}}}}{d_{\text{MgO}}}\right)^2 + \frac{\left(\delta_{R_{\text{pair}}}^2 + R_{\text{CoFeB}}^2\left(\frac{\delta_{d_{\text{CoFeB}}}}{d_{\text{CoFeB}}}\right)^2 + R_{\text{CoFeB}}^2\left(\frac{\delta_{k_{\text{CoFeB}}}}{k_{\text{CoFeB}}}\right)^2\right)}{(R_{\text{pair}} - R_{\text{CoFeB}})^2}}$$

As shown in **Table S2**, the uncertainty in k_{pair} decreases substantially when n increases from 10 to 20, since the increased n leads to higher R_{tot}. The increase in R_{tot} results in less error propagation due to the sources of uncertainties presented in **Table S3**.

S7. Gradient and Vertical-intercept Uncertainty Calculation

In **Figure 3b**, we plot R_{pair} measured from **[**CoFeB (1.2 nm)/MgO (d_{MgO})]$_{20}$ with d_{MgO} = 1.0, 1.3, and 1.6 nm, for both as-deposited and annealed samples with *T*BRs at top and bottom interfaces removed. We plot the best-fitted lines accounting for uncertainties in gradient and vertical-intercept, which are calculated based on the uncertainty in R_{pair}. This analysis essentially employs a Monte Carlo simulation to estimate the uncertainty in the linear regression parameters steaming from the uncertainty in the data points.

To quantify the gradient and vertical-intercept uncertainties, we assume that R_{pair} values follow a Gaussian distribution with a spread of 4 × standard deviation (σ), covering 99.99% of the data range. This is because the uncertainty of R_{pair} is the systematic uncertainty in our calculations rather than a random error in TDTR measurement. For each d_{MgO}, R_{pair} values are randomly generated from their Gaussian distribution. We plot best-fitted lines for these randomly generated values and record the corresponding gradient and vertical-intercept values. This procedure is repeated 10,000 times to obtain a comprehensive set of gradient and vertical-intercept values, which also follow a Gaussian distribution, as illustrated in **Figure S3**. The standard deviation (σ) of these distributions is taken as the uncertainty for both the gradient and vertical-intercept values in **Figure 3b**.

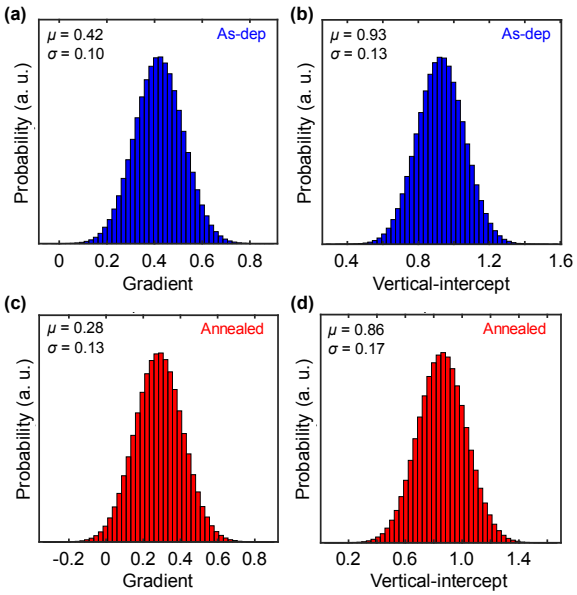

Figure S3. Probability distribution of gradient and vertical-intercept values for **(a-b)** as-deposited and **(c-d)** annealed samples, demonstrating Gaussian distributions. The mean (μ) and standard deviation (σ) of each Gaussian distribution are indicated on the respective plot.

S8. Impact of CoFeB Thermal Resistance

We measured the thermal conductivity of a 50 nm-thick as-deposited CoFeB film, which is 19.1 ± 0.6 $Wm^{-1}K^{-1}$. This low thermal conductivity for the CoFeB thin film ($k_{f,CoFeB} \approx 19.1$ $Wm^{-1}K^{-1}$) is due to the increased boundary scattering as the thickness reduces[7] from the bulk ($k_{b,CoFeB} \approx 87$ $Wm^{-1}K^{-1}$). An earlier study[8] on 1.0 nm CoFeB film found $k_e \approx 7.35$ $Wm^{-1}K^{-1}$ (electron contribution) at room temperature according to the Wiedemann–Franz law.[9-11] However, the total thermal conductivity of CoFeB thin film also includes a phonon contribution (k_{ph}), which cannot be measured independently. To estimate the total thermal conductivity of CoFeB ($k_e + k_{ph}$), we refer to previous measurements of 7.3 nm Pt film[12] which estimated that the lattice (phonon) contribution was of similar magnitude as the electrical contribution. We estimate the total thermal conductivity of CoFeB thin film from the literature to be ~14.7 $Wm^{-1}K^{-1}$. Thus, our estimate for 1.2 nm CoFeB thin film ($k_{f,CoFeB} \approx 19.1$ $Wm^{-1}K^{-1}$) is close to the reported literature data. We also assume $k_{f,CoFeB} \approx 19.1$ $Wm^{-1}K^{-1}$ for both as-deposited and annealed samples in our study, because CoFeB layers remain amorphous after annealing, which is shown in the above XRD analysis. Meanwhile, we note that the thermal resistance contribution of R_{CoFeB} is very small compared to R_{om} values [**Figure 3b**], thus our analysis of MgO k_{eff} is not sensitive to the assumption of $k_{f,CoFeB}$.

S9. Effective Thermal Conductivity of MgO

Table S4. Effective thermal conductivity of MgO (k_{eff}) with different MgO thickness (d_{MgO}) at room temperature, for both as-deposited and annealed samples.

d_{MgO} (nm)	k_{eff} ($Wm^{-1}K^{-1}$)
1.0 (As-dep)	0.70 ± 0.09
1.3 (As-dep)	0.85 ± 0.10
1.6 (As-dep)	0.95 ± 0.10
1.0 (Annealed)	0.85 ± 0.15
1.3 (Annealed)	1.00 ± 0.15
1.6 (Annealed)	1.19 ± 0.17

S10. Discussion of Experimental Methods

We note that we were unable to replicate the exact structure of industrial MTJs, where as-deposited MgO is typically crystallized on appropriate seed layers. This was due, in part because the TDTR measurement requires a certain thickness of the multilayer stack, with sufficient thermal resistance (vs. the Si substrate thermal resistance). Another constraint was imposed by the limitations of thin-film preparation in academic facilities. Nevertheless, our study emphasizes the critical role of thermal boundary resistance at the CoFeB/MgO interfaces. While the crystallinity of MgO in our samples may differ from that in industrial MTJs, the insights we provide are highly valuable for understanding thermal transport in ultrathin MgO tunnel barriers and improving thermal management in MRAM technology.

REFERENCES

(1) Giauque, W. F.; Meads, P. F. The Heat Capacities and Entropies of Aluminum and Copper from 15 to 300°K. *Journal of the American Chemical Society* **2002**, *63* (7), 1897-1901. DOI: 10.1021/ja01852a027.
(2) Liebing, N.; Serrano-Guisan, S.; Rott, K.; Reiss, G.; Langer, J.; Ocker, B.; Schumacher, H. W. Determination of spin-dependent Seebeck coefficients of CoFeB/MgO/CoFeB magnetic tunnel junction nanopillars. *J Appl Phys* **2012**, *111* (7). DOI: 10.1063/1.3679769.
(3) Touloukian, Y. S.; Buyco, E. H. *Thermophysical properties of matter - the TPRC data series. Volume 5. Specific heat - nonmetallic solids*; 1970.
(4) Xue, F.; Lin, S. J.; Song, M.; Hwang, W.; Klewe, C.; Lee, C. M.; Turgut, E.; Shafer, P.; Vailionis, A.; Huang, Y. L.; et al. Field-free spin-orbit torque switching assisted by in-plane unconventional spin torque in ultrathin [Pt/Co](N). *Nat Commun* **2023**, *14* (1), 3932. DOI: 10.1038/s41467-023-39649-1 From NLM PubMed-not-MEDLINE.
(5) Sood, A.; Cho, J.; Hobart, K. D.; Feygelson, T. I.; Pate, B. B.; Asheghi, M.; Cahill, D. G.; Goodson, K. E. Anisotropic and inhomogeneous thermal conduction in suspended thin-film polycrystalline diamond. *J Appl Phys* **2016**, *119* (17). DOI: 10.1063/1.4948335.
(6) Kwon, H.; Perez, C.; Park, W.; Asheghi, M.; Goodson, K. E. Thermal Characterization of Metal-Oxide Interfaces Using Time-Domain Thermoreflectance with Nanograting Transducers. *ACS Appl Mater Interfaces* **2021**, *13* (48), 58059-58065. DOI: 10.1021/acsami.1c12422 From NLM PubMed-not-MEDLINE.
(7) Chen, Y.-T.; Xie, S. M. Magnetic and Electric Properties of AmorphousCo40Fe40B20Thin Films. *Journal of Nanomaterials* **2012**, *2012*, 1-5. DOI: 10.1155/2012/486284.
(8) Hao, Q.; Xiao, G. Giant spin Hall effect and magnetotransport in a Ta/CoFeB/MgO layered structure: A temperature dependence study. *Phys Rev B* **2015**, *91* (22). DOI: 10.1103/PhysRevB.91.224413.
(9) Jonson, M.; Mahan, G. D. Mott's formula for the thermopower and the Wiedemann-Franz law. *Phys Rev B* **1980**, *21* (10), 4223-4229. DOI: 10.1103/PhysRevB.21.4223.
(10) Mahan, G. D.; Bartkowiak, M. Wiedemann-Franz law at boundaries. *Appl Phys Lett* **1999**, *74* (7), 953-954. DOI: Doi 10.1063/1.123420.
(11) Wilson, R. B.; Cahill, D. G. Experimental validation of the interfacial form of the Wiedemann-Franz law. *Phys Rev Lett* **2012**, *108* (25), 255901. DOI: 10.1103/PhysRevLett.108.255901 From NLM PubMed-not-MEDLINE.
(12) Yoneoka, S.; Lee, J.; Liger, M.; Yama, G.; Kodama, T.; Gunji, M.; Provine, J.; Howe, R. T.; Goodson, K. E.; Kennyt, T. W. Electrical and Thermal Conduction in Atomic Layer Deposition Nanobridges Down to 7 nm Thickness. *Nano Lett* **2012**, *12* (2), 683-686. DOI: 10.1021/nl203548w.